Ground performance of the High-Energy Focusing Telescope (HEFT) attitude control system

Kurt S. Gunderson, C. M. Hubert Chen, Finn Erland Christensen, William W. Craig, Todd A. Decker, et al.

Kurt S. Gunderson, C. M. Hubert Chen, Finn Erland Christensen, William W. Craig, Todd A. Decker, Charles James Hailey, Fiona A. Harrison, Ryan McLean, Ronald E. Wurtz, Klaus Ziock, "Ground performance of the High-Energy Focusing Telescope (HEFT) attitude control system," Proc. SPIE 5165, X-Ray and Gamma-Ray Instrumentation for Astronomy XIII, (3 February 2004); doi: 10.1117/12.513439

SPIE.

Event: Optical Science and Technology, SPIE's 48th Annual Meeting, 2003, San Diego, California, United States

Ground performance of the High-Energy Focusing Telescope (HEFT) attitude control system

Kurt Gunderson[a], C. M. Hubert Chen[d], Finn Christensen[b], William Craig[a], Todd Decker[a], Charles Hailey[c], Fiona Harrison[d], Ryan McLean[d], Ron Wurtz[a], Klaus Ziock[a]
[a]Lawrence Livermore National Laboratory, Livermore, CA, USA
[b]Danish Space Research Institute, Copenhagen, Denmark
[c]Columbia University, New York, NY, USA
[d]California Institute of Technology, Pasadena, CA, USA

ABSTRACT

The High Energy Focusing Telescope (HEFT) is a balloon-borne, hard x-ray/gamma ray (20-70 keV) astronomical experiment. HEFT's 10 arcminute field of view and 1 arcminute angular resolution place challenging demands on its attitude control system (ACS). A microprocessor-based ACS has been developed to manage target acquisition and sidereal tracking. The ACS consists of a variety of sensors and actuators, with provisions for 2-way ground communication, all controlled by an on-board computer. Ground based pointing performance measurements indicate 1σ jitter of 7″ and gyro drift rates of <1″ s^{-1}. Jitter is expected to worsen in the flight environment, but star tracker data are expected to reduce drift rates significantly, enabling a predicted 1σ absolute attitude determination of ≥4.7″. HEFT is scheduled for flight in Spring 2004.

Keywords: Balloons, attitude control systems, X-rays.

1. INTRODUCTION

Recent advances in depth-graded multilayer, grazing incidence optics[1] and high spatial resolution, CdZnTe detectors[2] are enabling dramatic improvements in the potential for hard X-ray astronomical missions. Because these technologies enable focusing at high X-ray energies, their implementation can achieve much higher angular resolution and sensitivity than what has been demonstrated with more traditional background-limited collimated (*e.g.* ASTRO-E2's HXD[3], RXTE's HEXTE[4]) and coded-aperture (*e.g.* INTEGRAL[5], Swift's BAT[6]) hard X-ray instruments. The High Energy Focusing Telescope[7] balloon-borne experiment (HEFT), scheduled for flight in Spring 2004, will be among the first of such missions to apply these advances over a bandpass of 20-70 keV.

HEFT has a half-power diameter (HPD) imaging performance of <1 arcminute[1] over a 10 arcminute[7] field of view (FOV.) This performance places challenging demands on the HEFT ACS, especially under the budget constraints of a balloon mission. First, targets must be acquired accurately enough to assure that x-ray emission is incident on, and remains incident on, the detectors. Furthermore, since the peak instrument response is attained on-axis, it is of particular interest to keep the x-ray images near the center of the detectors. Also, it is desirable that the jitter is low enough to enable real-time, relatively non-blurred detection and evaluation of images during flight without requiring full aspect reconstruction. Additionally, on-board sensors must measure jitter well enough to enable the application of accurate aspect solutions to time-tagged photon lists during the post-flight analysis. Finally, the ACS must provide fully autonomous operations in case of loss of communications during flight and for eventual use in Long and Ultra Long Duration Balloon missions, during which continuous communication is not possible. Our initial goals in designing the HEFT ACS were:

- ±3′ absolute attitude accuracy.
- ≤6″ RMS aspect reconstruction accuracy.
- ≤20″ RMS jitter.
- >24 hr autonomous operation capability.

We have developed an ACS that has met these specifications during ground testing. In this paper we present a description of the ACS system, the balloon gondola itself, the results of initial ground tests, and the predicted in-flight performance.

X-Ray and Gamma-Ray Instrumentation for Astronomy XIII, edited by Kathryn A. Flanagan, Oswald H. W. Siegmund, Proceedings of SPIE Vol. 5165 (SPIE, Bellingham, WA, 2004)
0277-786X/04/$15 · doi: 10.1117/12.513439

2. HARDWARE

HEFT consists of an array of grazing incidence, nested shell optics modules and one CdZnTe detector per module. All optics module/detector pairs are coaligned and fixed in the same altazimuth mount, which hangs from a single balloon line. The local gravity vector through the connection to the balloon line defines the azimuthal (AZ, or more accurately, -*yaw*) axis, and everything below the connection to the balloon line rotates as a unit during AZ rotations. To enable the observation of targets at and around zenith, whose images otherwise would be vignetted by balloon connection hardware, the altitude, or *pitch,* axis (hereafter referred to as the elevation, or EL axis) does not pass directly through the AZ axis. Therefore, $60° \leq EL \leq 90°$ can be observed on one side of the hook and $0° \leq EL < 60°$ can be observed on the other side of the hook, all over $0° \leq AZ < 360°$. As a result, the entire local sky is accessible at all times. Figure 1 shows a photograph of the gondola as it hangs in the laboratory, with two rotation axes, two of the four actuators, and the hermetically sealed electronics vessel identified.

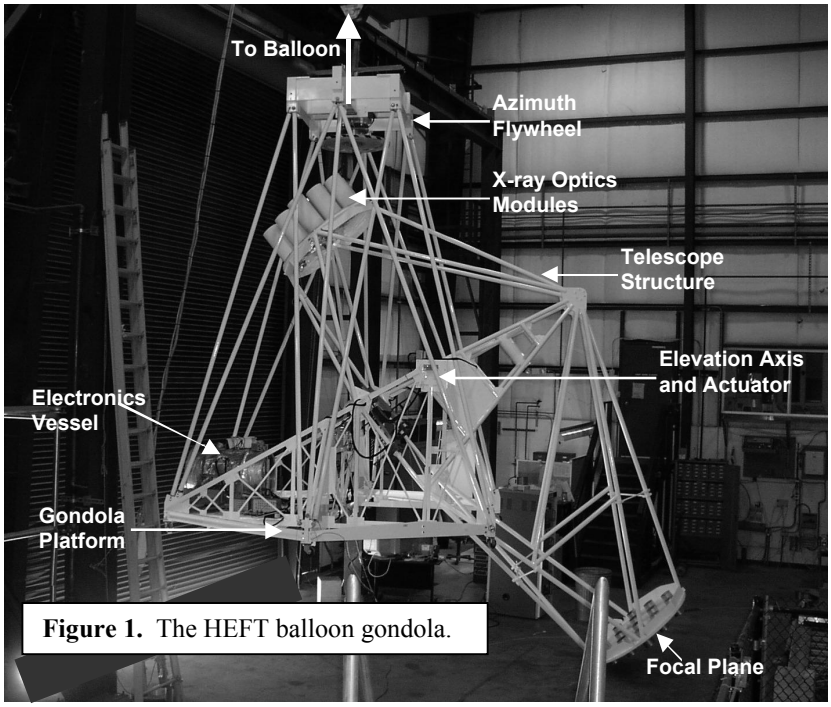

Figure 1. The HEFT balloon gondola.

The four actuators used to drive gondola motions on HEFT were inherited from the GRATIS[8] balloon experiment. They include a telescope EL torque motor, an oscillation-damping motor, an AZ motor, and a gondola-balloon coupling motor. The EL torque motor drives the motions of the main telescope structure, to which the optics modules and detectors are mounted, relative to the gondola platform. The oscillation-damping motor drives a reaction wheel whose normal lies along the **EL×AZ≡ROLL** axis (or **yaw×pitch=roll** axis), and is used to damp pendulum motion around this axis. The AZ motor applies torque to a reaction wheel whose normal is aligned with the AZ axis in order to drive gondola platform azimuthal motions. Although this actuator provides excellent fine control over the AZ position, the reaction wheel rotation saturates at approximately 100 RPM. This rate is reached quickly while slewing, and more slowly during star tracking operation. Therefore, the gondola-balloon coupling motor is used to transfer this buildup of angular momentum out of the reaction wheel by applying torque to the balloon against the gondola.

A variety of sensors, oftentimes providing redundant attitude information to the system, are mounted to the gondola platform and telescope structure. Table 1 lists the sensors used, identifies their sensitive axes, and indicates their mount locations and electrical interfaces. The EL sensitive axes are demarcated according to three categories. (1) Platform EL. This is the position of the gondola platform alone relative to the local gravity vector, and will oscillate around zero. (2) Relative EL. This is the EL position of the telescope structure relative to the gondola platform. (3) Absolute EL. This is the sum of (1) and (2), and is essential for knowledge of telescope pointing in astronomical coordinates. Since gyro #2 is mounted on the telescope structure, its non-EL sensitive axis lies in the AZ-ROLL plane, offset from the ROLL axis by the angle EL. In order to assure that the balloon, through which x-rays will pass, does not obscure visible starlight from both

star trackers simultaneously, one star tracker is mounted askew from the x-ray optical axis by approximately 30° and the other is coaligned with the x-ray axis.

One two-way and three one-way radio frequency (RF) channels transmit data between the gondola and the ground station. 600 bytes of ACS housekeeping data are transmitted to the ground per second as an RS-422 asynchronous 38.4

Table 1. HEFT sensor list.

	SENSITIVE AXES				
SENSOR	AZ	EL	ROLL	MOUNT LOCATION	INTERFACE
Gyro #1: Litton G-2000	×		×	Gondola platform	Analog
Gyro #2: Litton G-2000	×[d]	×[a]	×[d]	Telescope structure	Analog
Rotary encoder (2): Gurley A25S		×[b]		Gondola platform/telescope structure interface	Digital
Magnetometer (2): Watson FGM301/99	×			Gondola platform	Analog
GPS: Trimble TANS Vector	×	×[c]	×	Gondola platform	RS-422
Star tracker #1	×	×[a]	×	Telescope structure (on-axis)	Ethernet
Star tracker #2	×	×[a]	×	Telescope structure (off-axis)	Ethernet
Accelerometer: Crossbow TG series		×[a]	×	Telescope structure	Analog

[a,b,c]Denotes absolute, relative or platform elevation, respectively

[d]The actual sensitive axis lies in the AZ-ROLL plane.

kbit s^{-1} binary stream that is modulated into a 420-440 MHz RF band. These data include time-stamped attitude data, sensor data, and a variety of status bits. ACS and primary science detector module uplink commands are transmitted from the ground as an RS-422 9.6 kbit s^{-1} binary stream that has been modulated into a 406-420 MHz band. An additional uplink channel, which is used to reset hardware by toggling relays, carries an RS-232 1.2 kbit s^{-1} binary stream that has been modulated into the 420-440 MHz band. For the sake of redundancy, the asynchronous RS-422 460.8 kbit s^{-1} binary data stream from the primary science detector module is both stored on-board the gondola during flight and modulated into a 2.3 GHz band downlink. Finally, images from the two star tracker cameras and a variety of monitor cameras are multiplexed into a single UHF video downlink.

As depicted in the schematic diagram in Figure 2, a PC/104 single board computer (SBC) stack lies at the center of the

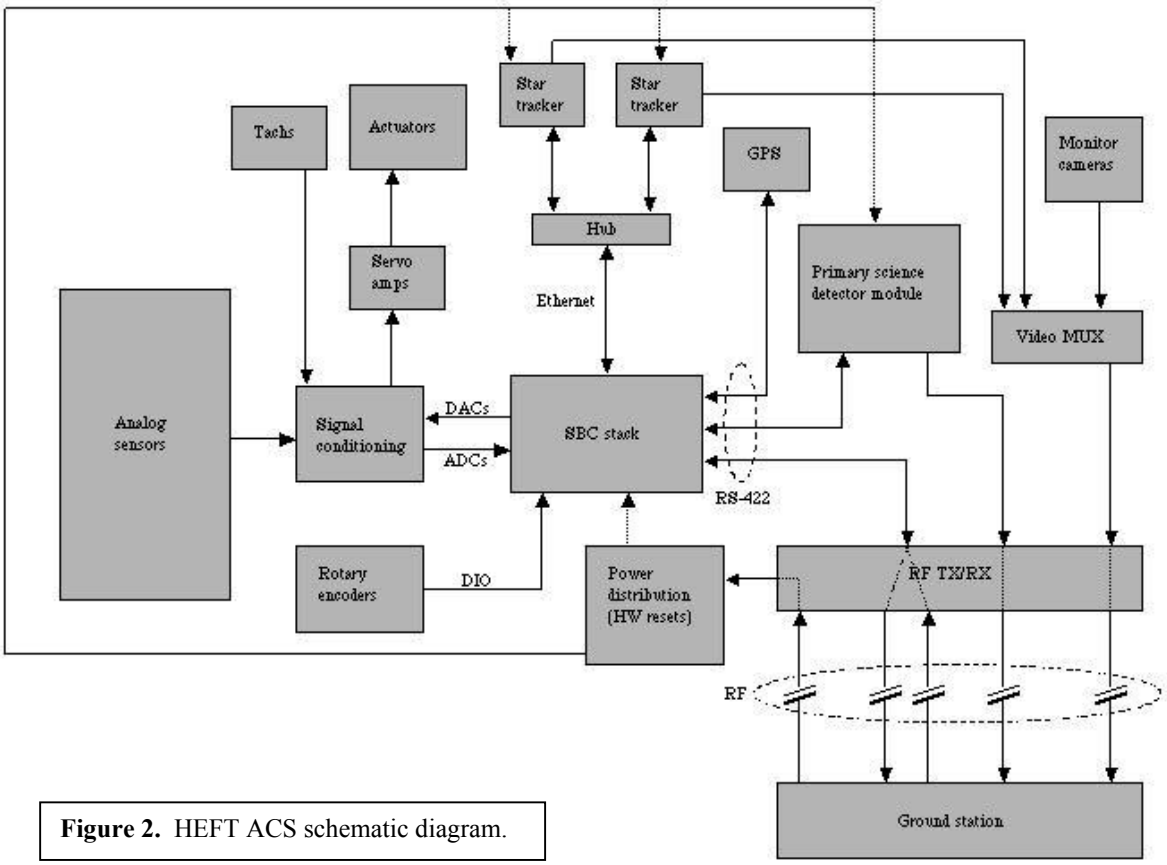

Figure 2. HEFT ACS schematic diagram.

actuators, sensors, and communications lines. A 450 MHz central processing unit (CPU; Advanced Microperipherals Tiny786LP) drives an ethernet adapter chip, two RS-232 serial ports, redundant 10 GB integrated drive electronics (IDE) hard disks, and four input/output (IO) cards that are stacked along the Industry Standard Architecture (ISA) bus. The ethernet port links the CPU to the two star tracker units via a 10 Base-T hub. Both the ACS housekeeping telemetry stream and the primary science detector module binary stream are written locally to both of the IDE disks. Included in the IO card stack is a serial adapter card (ConnectTech Xtreme Opto/104) with four optically-isolated high-speed (up to 460.8 kbit s^{-1}) RS-422/RS-232 configurable serial ports, and three multi-IO cards (Diamond Systems MM-32). The serial ports carry data between the CPU and the GPS-based attitude navigation system (RS-422 38.4 kbit s^{-1}), the primary science detector module (RS-422 460.8 kbit s^{-1}), and the demodulated up/downlink lines described earlier. The multi-IO cards each include 32 16-bit analog-to-digital converters (ADCs), 4 12-bit digital-to-analog converters (DACs), and 3 8-bit words of digital input/output (DIO). Analog inputs pass through signal conditioning electronics that set levels to fall within the ±10 V ADC range over the signals' regions of interest, and that provide low pass resistor-capacitor (RC) filtering to attenuate high frequency noise. Analog output signals pass through isolation amplifiers before reaching RC filters in the servo amplifiers.

In order to take advantage of heat distribution by convection, a sealed pressure vessel houses the SBC stack, hard disks, ethernet hub, signal conditioning electronics, and power distribution box. This vessel is identified in Figure 1. Similarly, independent pressure vessels house both gyros, the accelerometer, and the star tracker units. The central point of a star ground system is located within the main pressure vessel, and all cables external to the pressure vessel are shielded.

3. SOFTWARE

At the core of the ACS, custom software provides a digital implementation of a control feedback loop. The software is written in the C programming language under the QNX 6.1.0 real-time operating system (RTOS) to do the following:

- Determine attitude from sensor inputs.
- Drive the actuators.
- Maintain local data storage.
- Manage communications with the ground station.

A priority-driven, multi-threaded software architecture takes advantage of the QNX RTOS's reliability, speed, apparently seamless context switching, and, most importantly, timing control, to manage all these tasks simultaneously. Following a description of the software flow, each of the ACS performance-critical bulleted items will be detailed.

3.1 SOFTWARE FLOW

A software flow diagram is shown in Figure 3 with periodic and intermittent events labeled. Upon system startup the flight executable launches automatically. Initializations include IO board configuration, GPS system checks, file and communication port creation, the loading of the flight target program, and creation of the socket server for star tracker communication. Then a 100 Hz software timer starts to trigger attitude update events in a main attitude control loop. In order to reduce the ≈1.5 mV RMS analog noise in the system, voltages from the analog sensors are read every 10 ms, but samples are averaged and processed every 100 ms. Thus, attitude errors are determined at 10 Hz. Also at 10 Hz, actuator control voltages are adjusted and a single housekeeping downlink data packet (60 bytes) is transmitted to the ground station. Every second memory buffers holding the transmitted housekeeping data are written to disk. The GPS system and the star trackers output data as soon as they are available, which is approximately 1 second and 5 seconds, respectively. Uplink commands and science data arrive intermittently and, like the GPS and star tracker data, are processed immediately upon receipt.

Although using a single CPU to manage many tasks simplifies the system hardware, it introduces the concern that computational limits might be exceeded. Thus a software stopwatch within every thread monitors the processor time that the functionality within those threads consumes. As the total time consumed approaches the time available, processor congestion degrades performance and can cause system failures. Table 2 outlines typical times consumed by the various threads over the course of a second. Science data rates are for the Crab Nebula, which is a bright source: Typically count rates will be lower. Also, uplink commands are unlikely to be sent at 1 Hz. Thus the 58% processor burden is likely an overestimate of the true burden. Performance degradation starts to become apparent at the 85-90% level.

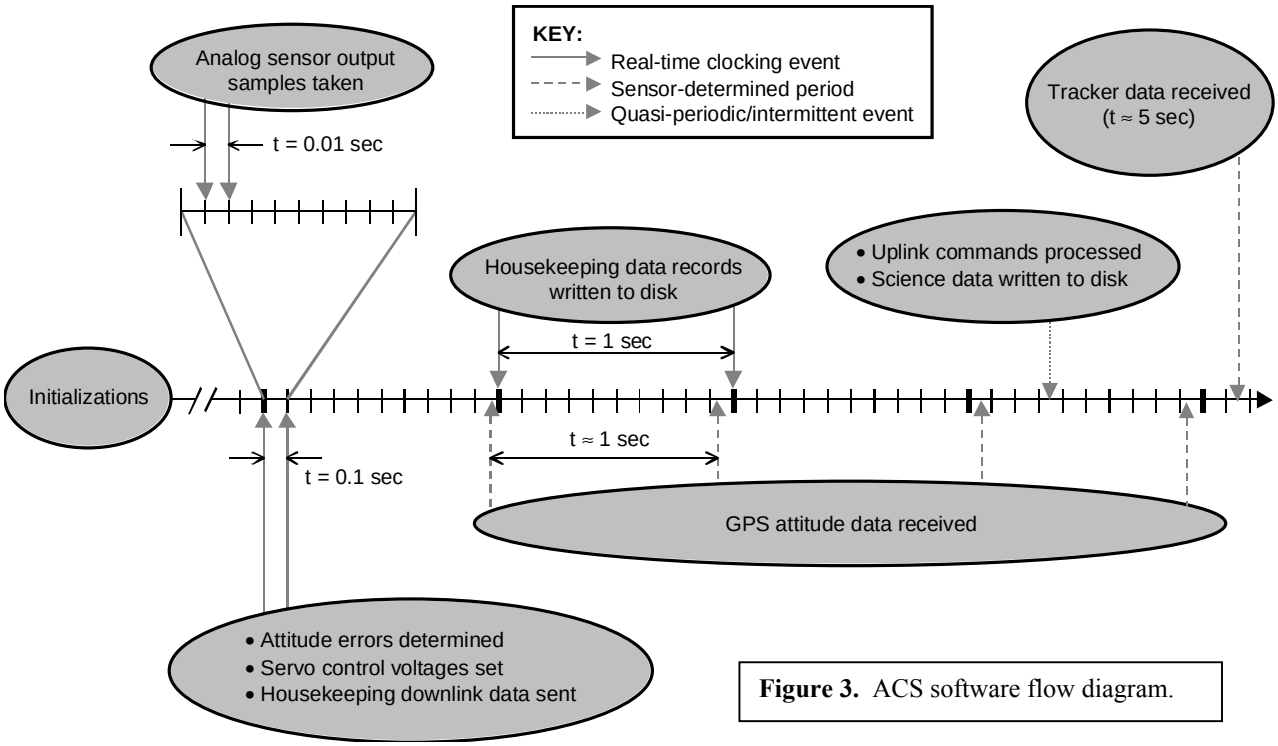

Figure 3. ACS software flow diagram.

Table 2. HEFT ACS CPU time budget.

THREAD FUNCTION	PROCESSOR TIME CONSUMED (ms s^{-1})
ADC/DAC/DIO reads/writes	200
Housekeeping downlink + local storage	155
Uplink commands (at 1 command s^{-1})	6
GPS communication	2
Star tracker communication	<1
Science data receipt + storage (detector^{-1})	22[a]
Processor power consumed (10 detectors)	58%

[a]For the Crab Nebula, a bright hard x-ray source.

3.2 ATTITUDE DETERMINATION

The primary method used to determine attitude is to constrain sensor data that is accurate in the short-term with absolute attitude fixes that, though more reliable, arrive infrequently. Specifically, rapidly-sampled gyro outputs provide excellent short-term rotation rate accuracy, but integration of their output signals introduces two problems: First, an uncertain integration constant must be chosen. Second, systematic voltage measurement errors lead to a misperception of motion and result in gyro drift. Conversely, the star trackers do not provide data at a sufficient rate to control attitude over the short-term, but they provide accurate absolute attitude fixes as star pattern matches are found. Thus the star trackers' absolute fixes can be used to set the gyro algorithms' integration constants and control gyro drift while the gyro data are used to interpolate between star tracker readings. The result is both accurate short-term and long-term attitude knowledge.

Additionally, redundant attitude information is available around all axes for both the short-term and long-term classifications of sensors. Because simply selecting and using the most accurate sensor data for each axis would discard valuable information from the less-accurate sensors, a filter algorithm is used to combine similar readings in statistically weighted averages. For example, an average of lightly weighted, less accurate GPS (plus rotary encoder in the case of EL determination) and heavily weighted, more accurate star tracker readings constrains the absolute gyro-determined attitude over long-terms. Similarly, over the short term, the gyros themselves provide information on a fourth axis, which lies in the AZ-ROLL plane by an offset angle of EL. This rate information is split into AZ and ROLL components, lightly weighted according to the errors introduced by the EL decoupling, and averaged against the more accurately gyro-determined AZ and ROLL rates. Magnetometers, too, provide AZ information with a sensitivity of 20″. Unfortunately, magnetometers can introduce large systematic errors in absolute AZ due to uncertainties and variability in the Earth's magnetic field[9]. For example, sub-surface mineral deposits can divert the local magnetic field from model predictions by tens of arcminutes, and magnetic storms can divert it by a degree or more, rendering the magnetometers' absolute readings unreliable for HEFT. However, during the expected exposure duration during flight, the field offsets are likely to remain constant to within ≈1′. Therefore, magnetometer AZ readings are differentiated into AZ rates, integrated over time, corrected for random walk drift by the GPS/star tracker absolute AZ heading, and combined with gyro AZ in weighted averages.

Overcoming the systematic gyro output voltage measurement errors requires accurate knowledge of gyro bias voltages, which can vary by as much as 10 mV between startups. Bias voltage is the output voltage of a gyro axis that is perfectly still. Since output voltage is interpreted as being proportional to the rate of gyro rotation around a particular axis, the software would interpret a non-zero bias voltage as a real motion and infer that the platform to which the gyro is mounted is undergoing a steady motion around that axis (10 mV → 7.2″ s^{-1}). This systematic source of attitude error contributes to what is known as gyro drift. To reduce drift rates, bias voltages must be measured and subtracted from the inputted voltage values within the software. Thus, during the first 20 sec of loop operation, while the gondola is still on the ground, initial gyro bias voltages are measured: Corrections for earth rotation are applied to the gyro output rates, all residual "motions" are attributed to bias voltages, and a leaky average of these biases is kept until the measurement converges. The upper plot in Figure 4 demonstrates the convergence of these algorithms for one gyro axis. At t=0, the software launches, presuming a grossly errant bias voltage value. Within 15 s the bias measurement is steady to within 1 mV.

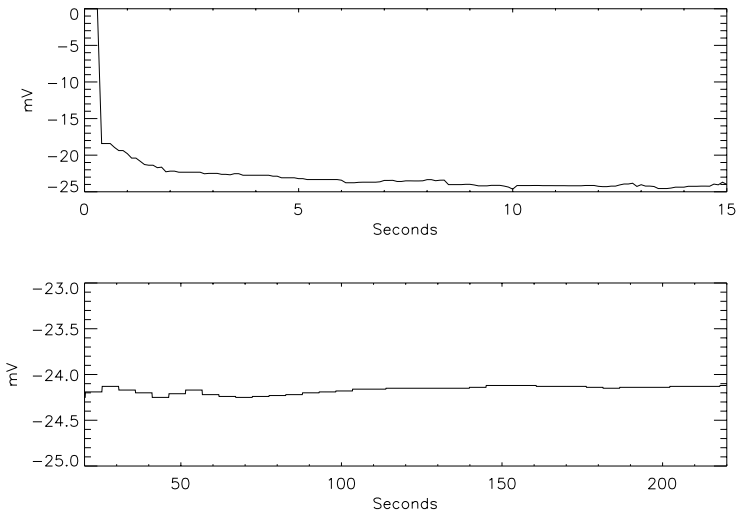

Figure 4. Convergence of the initial gyro bias measurement (*upper*) and longer term gyro bias measurement (*lower*).

Since environmental changes, especially temperature, lead to gyro bias variance, the bias must be measured continually throughout flight. Due to dissimilarities in mounting positions and degrees of rotational freedom, different approaches are taken for the various attitude axes. The only means of determining AZ bias is with GPS/star tracker absolute AZ data. As absolute fixes arrive from those systems, discrepancies between the absolute fixes and gyro readings are presumed to be due to bias errors, and the bias voltage used to interpret the gyro signal is adjusted accordingly. ROLL motions, however, only occur as oscillations around a fixed zero position that is defined by the local gravity vector. Over many oscillation periods, an average ROLL position is thus expected to be near zero. Therefore, departures from a zero average value are presumed to be a result of bias errors. The lower plot of Figure 4 demonstrates the stability of this approach. To the left of the plot, apparent bias oscillations arise from poor averages that were computed during an episode of heavy (>10′ peak-to-peak) oscillation. As a result, bias corrections are not applied while pendulum motion is strong. However, as the oscillations damp, the bias measurements stabilize. The gradual bias rise across the plot is real, and is due to a temperature rise as the gyro warms up with use. Gyro-detected EL motions are subject to both

pendulation and telescope motions. Thus a ROLL-like approach, coupled with rotary encoder readings, can be used, but GPS/star tracker fixes are more accurate.

3.3 ACTUATOR CONTROL

One of two algorithms, selected according to the magnitude of the pointing error, determines the control voltage settings for the AZ and EL actuators. When errors are large (greater than 2°), the gondola is said to be in the *slewing zone*. In the slewing zone, rapid motions are desired. Thus a fixed, strong torque is applied to the motors. One caveat, however, is gyro saturation. The Litton G-2000 gyro servo boards have been modified to provide ±10 V output at a gain of $0.2° \ s^{-1} \ V^{-1}$. Therefore rotation speeds $>2° \ s^{-1}$ cause bad gyro signals and a loss of absolute gyro attitude knowledge. Consequently, torque is applied to an actuator to oppose motions that approach these rates. When AZ errors place the gondola in the slewing zone, the coarse momentum-dumping AZ actuator drives the motion. This is because the AZ reaction wheel reaches its maximum rate quickly, at which point its motor can no longer provide torque to the gondola. However, the angular momentum that builds up in the reaction wheel helps brake the gondola when it passes into what is referred to as the *tracking zone*. Once in the tracking zone, control is turned over to individual proportional, integral, and derivative (PID) control algorithms for both AZ and EL axes.

Only one algorithm is used to govern torque in the oscillation-dumping actuator. This algorithm attempts to transfer gondola angular momentum in to a reaction wheel by simply opposing the detected ROLL motions.

4. GROUND TESTING

Nighttime ground testing of the ACS has been performed at Lawrence Livermore National Laboratory (LLNL) using all four actuators. During testing, the gondola hung from a bridge crane near a tall high-bay door. Because the crane's hook would otherwise have let the momentum-dumping actuator spin freely, the actuator was connected via a pulley to weights against which it could apply torque. The response of this system was adjusted to simulate the known stiffness of the cable ladder used to suspend the gondola below the balloon. Although the star tracker could view a 60° span of southern sky in AZ and a 30° span of sky in EL when the high-bay door was open, the magnetometers and GPS were not useful. Magnetic fields within the building saturated the magnetometer outputs, and no GPS fix was possible from inside. Consequently, attitude was determined solely from the gyros, rotary EL encoders, and the coaligned star tracker. Additionally, software to close the star tracker/gyro feedback loop had not been installed. Therefore gyro biases were not measured after the first 20 s except for the gyro ROLL axis, and the initial attitude values used for the gyros were estimated by eye. Initial estimates were accurate enough to acquire stars repeatedly into the star tracker's ≈2° FOV and subsequently track their sidereal motions. RF communication was not used. Instead, an RS-232 serial line connected the up- and downlink ports from the gondola's control CPU directly to the ground support equipment (GSE) computer. GSE software received and displayed downlink data, and allowed the user to send uplink commands. Although it was not essential for operating the system, an ethernet line from the gondola to a GSE hub enabled telnet sessions to monitor the control CPU, and a mouse, keyboard, and display GSE cable enabled direct operation of the coaligned star tracker computer. Rack mounted DC power supplies provided power to the gondola instead of flight batteries. All cabling was run so as to minimize torques on the gondola as it slewed.

Two parameters that characterize the ACS performance are drift, which was described above, and jitter. Jitter is a relatively high frequency pointing error that is affected by electrical noise, the intrinsic mechanical responses of the gondola to its actuators, and external environmental influences like wind. Electrical noise leads to sensor voltage read errors, which in turn lead to attitude calculation errors and then tracking errors. As an example of an intrinsic mechanical system limitation, driving EL motions applies reverse torque to the gondola frame. Since the moment of inertia (MOI) of the telescope is comparable to the MOI of the gondola frame, this torque excites detectable pendulum motion in the gondola frame ($\tau \approx 5$ s). The damping timescale of the oscillations (see Figure 5) exceeds the reaction time of the telescope so, unless measures are taken to damp them, the oscillations must be accepted as an unavoidable source of pointing error.

Pendulum motion of the gondola platform introduces attitude error in EL and ROLL. In addition to being driven by actuator torque, these oscillations can be driven by wind. Therefore the damping reaction wheel has been added to the system to reduce ROLL motions. Figure 5 demonstrates the benefits of this addition. The two sets of plotted data represent ROLL positions versus time after pendulum motions had been excited by the reaction wheel itself, whose gain

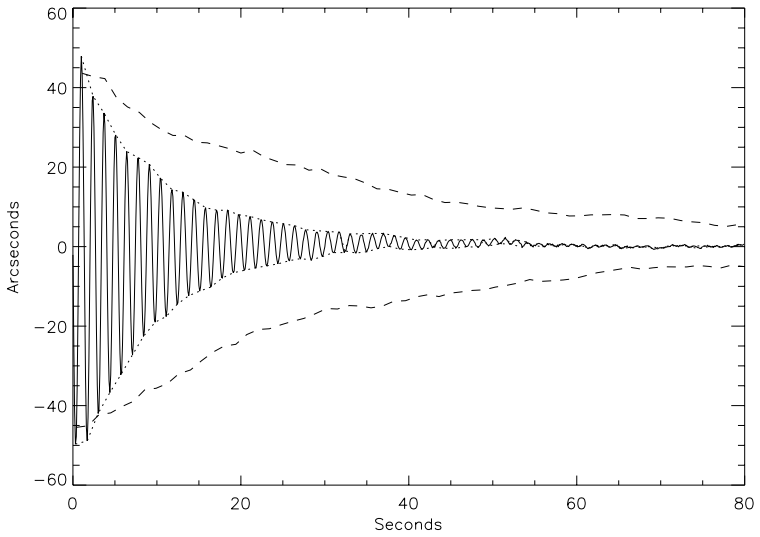

Figure 5. ROLL oscillation damping with and without the flywheel.

had been reversed via GSE control. When peak-to-peak (PP) magnitudes exceeded 1′ excitation was stopped with a GSE command. At this point the reaction wheel gain was either reversed and used to damp the motion, or disabled such that the gondola was left to swing freely. The solid line represents the ROLL trajectory for the damped case. Its decay envelope is overplotted as a dotted line. For the sake of clarity the undamped trajectory has not been overplotted, but its envelope is shown as a dashed line. The benefits of the damping reaction wheel are obvious. Within 25 seconds the PP magnitude reaches 10″ in the damped case, whereas the undamped case requires 80 seconds to reach this level.

Figure 6 shows a plot of gyro-determined AZ and EL pointing errors for 1000 seconds of star tracking data sampled at 10 Hz. Because the gondola's response to wind on the ground, and the wind itself on the ground, is unlikely to be the same as that at 40 km altitudes where air density is lower and flow dynamics are different, measurements were made with the high-bay door closed. Thus the measured jitter represents system-intrinsic jitter and, unless system modifications are made to reduce it, represent the best-case ACS performance. The data demonstrate an RMS pointing error of 6.9″. Typical electrical noise on the gyro outputs is 4 mV RMS, which contributes 0.28″ RMS of attitude error for a 10 Hz update frequency. Therefore, the observed jitter is dominated by the gondola's mechanical response. However, the high instantaneous accuracy of the gyros will enable the application of aspect solutions to the time-tagged x-ray photon list to reduce ACS blur post-flight. Since the pointing errors in Figure 6 were determined by the gyros, whose time-integrated rates are unaware of yet vulnerable to their own bias errors, the drift component is not evident. Detecting drift requires the use of an absolute reference attitude and has been provided by the coaligned star tracker.

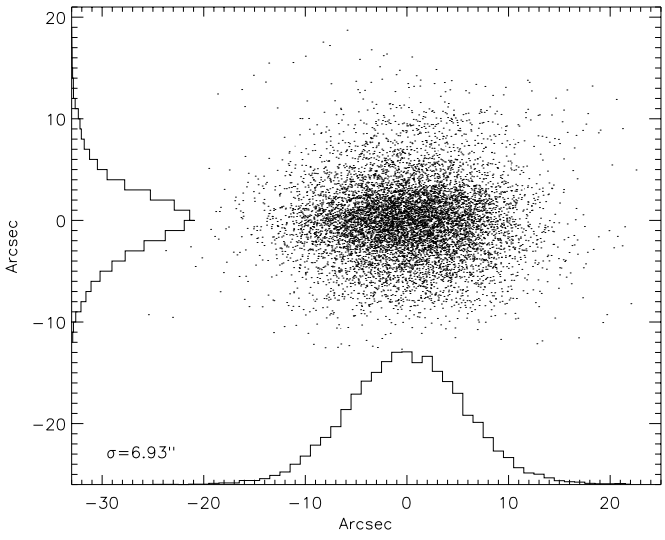

Figure 6. Pointing error according to gyros.

Drift has been measured with a 31 minute long data set by comparing the gyro-measured attitude with star tracker attitude fixes whenever the star tracker fixes arrived, which was every 5.8 seconds on average. The drift trajectory is shown in Figure 7. Differences between gyro and star tracker attitude values primarily arise from gyro noise, star tracker inaccuracy, and gyro drift. To decouple these sources of error a second order polynomial was fit to the differences as a function of time. The first order term is interpreted as gyro drift, the second order term is interpreted as rate of change of gyro drift, and residuals of the fits are attributed to gyro and star tracker inaccuracy added in quadrature. Measured drift rates are 0.38 and 0.79″ s^{-1} for AZ and EL, respectively, and rates of change of drift are 0.13 and 0.19″ s^{-1} hr^{-1}. Residuals of 9.5 and 8.9″

RMS for AZ and EL, respectively, are dominated by star tracker inaccuracies, which most likely arise from the star-finding algorithm's attempts at finding centroids of star images that have been distorted by platform jitter. Since the gondola swings with a pendulum period of approximately 5 seconds and CCD exposure times were 1 second, star images' point spread functions were distorted from nominally symmetric shapes into streaks.

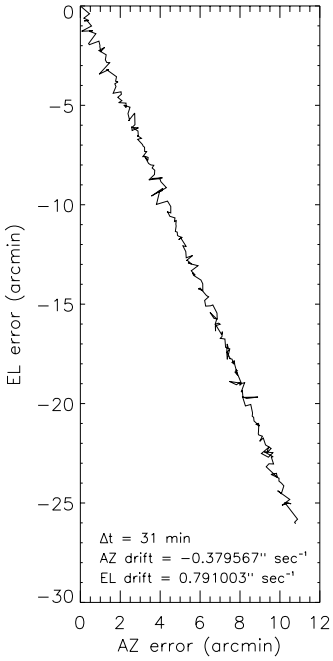

Figure 7. Gyro drift trajectory.

Although a single star tracker solution alone cannot constrain gyro-determined absolute pointing knowledge at the 6″ pointing accuracy requirement, many solutions can be averaged to reduce errors and meet that goal. However, the number of samples used per average must be chosen carefully to maximize pointing accuracy: The more samples that are used, the more the gyro drift will degrade pointing accuracy while the averaged data set is taken. Thus running averages of the drift rates as well as the absolute pointing must be kept. Again, the more samples used to constrain drift, the more the gyro bias changes will degrade the drift measurements' accuracy while the drift-determining data set is taken. However, second order and higher time derivatives of gyro/star tracker pointing discrepancies are neglected. As demonstrated by Figure 8, convergence to the pointing accuracy requirement should be possible without it. Figure 8 shows predicted pointing error contours in arc seconds against numbers of samples averaged in the gyro drift measurement (N_{drift}) and the absolute pointing measurement (N_{pointing}). The previously reported drift change rate (≈0.23″ s^{-1} hr^{-1}) is presumed to degrade both drift measurements and therefore absolute pointing measurements over time, and the drift rate is presumed to degrade the absolute pointing measurement over time. This plot predicts peak ACS performance of 4.7″ RMS absolute pointing accuracy at

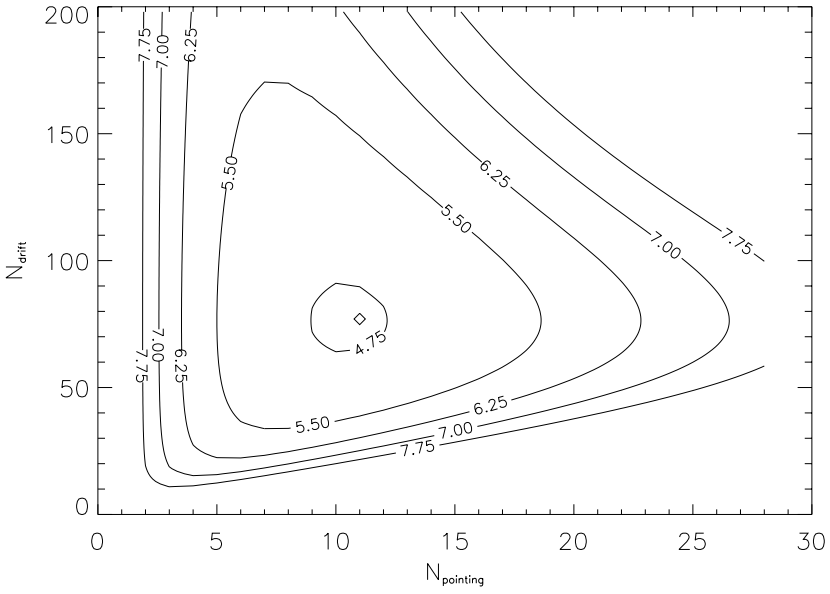

Figure 8. Predicted pointing error contours in arcsec for the number of tracker samples used to constrain absolute pointing (N_{pointing}) and gyro drift (N_{drift}).

$N_{pointing}$=11 and N_{drift}=77. Convergence on 6″ accuracy is expected after 25 solutions, or 145 seconds at current star tracker periods.

Since upcoming software improvements are expected to reduce star tracker periods significantly, performance is likely to improve. Furthermore, for some targets, both star trackers will have unobstructed views of the sky during flight, halving the effective tracker period. For an effective star tracker period of 2.0 seconds, convergence on 6″ accuracy is predicted after 50 seconds with a peak ACS performance of 3.3″ RMS .

5. CONCLUSION

We have presented the attitude control system of the HEFT high-altitude balloon experiment. The HEFT ACS primarily uses signals from gyros and star trackers to drive four actuators around three rotation axes. Data from additional sensors provide redundant information for error checking, reliability, and improved attitude knowledge. ACS ground testing has demonstrated 6.9″ RMS jitter and 0.88″ s^{-1} gyro drift. Although jitter measurements were made with the gondola protected from wind, gyros will be sensitive to this jitter, and therefore gyro data can be used to apply aspect corrections after flight. Gyro drift corrections will rely on absolute attitude fixes by at least one of two star tracker systems. Ground testing of a star tracker system indicates a 13″ RMS measurement accuracy at a solution return period of 5.8 seconds while the gondola was vulnerable to wind gusts. After 450 seconds of star tracker solutions, absolute attitude knowledge is predicted to converge to an accuracy of 4.7″ RMS using one of two star tracker systems after the gyro/star tracker loop is closed. After 145 seconds the accuracy is predicted to converge to an accuracy of 6″ RMS, the mission requirement.

Although these results are promising, they must be viewed with some caution. First, the 6.9″ RMS jitter measurement was made in a closed room with minimal air currents, which will affect operations during flight. The 13″ RMS star tracker accuracy likely reflects performance degradation due to wind-induced oscillations. At float altitudes, ≈40 km, the wind speeds can be as high as 50-70 km hr^{-1}, but pressures are much lower than on the ground. Past experience with the GRATIS gondola showed a degradation of a factor of ~2 at float altitudes as compared to ground performance. Final ACS validation awaits the upcoming flight in Spring 2004.

ACKNOWLEDGEMENTS

Mechanical construction of the instrument was supported by R. Hill and D. Carr of LLNL. The electronics were designed by D. Deane of LLNL. This work was performed under the auspices of the U.S. Department of Energy by the University of California, Lawrence Livermore National Laboratory under Contract No. W-7405-ENG-48.

REFERENCES

1. J. E. Koglin, F. E. Christensen, J. Chonko, W. W. Craig, T. R. Decker, M. A. Jimenez-Garate, K. Gunderson, C. J. Hailey, F. A. Harrison, C. P. Jensen, M. Sileo, D. L. Windt, and H. Yu, "Development and production of hard X-ray multilayer optics for HEFT," *Proc. SPIE*, **4851**, pp. 607-618, 2003.
2. F. A. Harrison, A. E. Bolotnikov, C. M. H. Chen, W. R. Cook, P. H. Mao, and S. M. Schindler, "Development of a high-spectral-resolution cadmium zinc telluride pixel detector for astrophysical applications," *Proc. SPIE*, **4851**, pp. 823-830, 2003.
3. I. Hajime, "Astro-E2 mission: the third x-ray observatory in the 21st century," *Proc. SPIE*, **4851**, 289-292, 2003.
4. R. E. Rothschild, P. R. Blanco, D. E. Gruber, W. A. Heindl, D. R. MacDonald, D. C. Mardsen, M. R. Pelling, L. R. Wayne, and P. L. Hink, "In-flight performance of the high-energy x-ray timing experiment on the Rossi x-ray timing explorer," *Ap. J.*, **496**, pp. 538-549, 1998.
5. C. B. Wunderer *et al.*, "Imaging with the coded aperture gamma-ray spectrometer SPI aboard INTEGRAL," *Proc. SPIE* **4851**, pp. 1269-1280, 2003.
6. S. D. Barthelmy, "Burst alert telescope (BAT) on the Swift MIDEX misssion," *Proc. SPIE*, **4140**, pp. 50-63, 2000.
7. F. A. Harrison, S. E. Boggs, A. Bolotnikov, F. E. Christensen, W. R. Cook, W. W. Craig, C. J. Hailey, M. Jimenez-Garate, P. H. Mao, S. E. Schindler, and D. L. Windt, "Development of the high-energy focusing telescope (HEFT) balloon experiment," *Proc. SPIE*, **4012**, pp. 693-699, 2000.
8. M. Seiffert, P. Lubin, C. J. Hailey, K. P. Ziock, and F. A. Harrison, "The gamma-ray arc-minute imaging system (GRATIS) - Mechanical design and expected performance," *Proc. SPIE*, **1159**, pp. 344-353, 1989.

9. F. J. Lowes, “An estimate of the errors of the IGRF/DGRF fields 1945-2000,” *EP&S*, **52**, pp. 1207-1211, 2000.
10. W. W. Craig, R. McLean, and C. J. Hailey, “Sub-arcminute pointing from a balloon borne platform,” *Proc. SPIE*, **3365**, pp. 87-97, 1998.